CFD MODELING OF A SYNTHETIC JET ACTUATOR

Marouane Dghim*, Maher Ben Chiekh* and Ben Nasrallah Sassi
LESTE-Laboratoire d'Etudes des Systèmes Thermiques et Energétiques
National Engineering School of Monastir
Ibn El Jazzar Avenue, P.O. Box 5019, Monastir, Tunisia
(*Corresponding authors: maher.benchiekh@enim.rnu.tn , dghim.aircraft@gmail.com)

ABSTRACT. Synthetic jet actuators show good promise as an enabling technology for innovative boundary layer flow control applied to external surfaces, like airplane wings, and to internal flows, like those occurring in a curved engine inlet. The appealing characteristics of a synthetic jet are zero-net-mass –flux operation and an efficient control effect that takes advantages of unsteady fluid phenomena. The formation of a synthetic jet in a quiescent external air flow is only beginning to be understood and a rational understanding of these devices is necessary before they can be applied to the control of flows outside of the laboratory. The synthetic jet flow generated by a planar orifice is investigated here using computational approach. Computations of the 2D synthetic jet are performed with unsteady RANS modeled with the Realizable $k-\varepsilon$ turbulence model available in FLUENT environment. In this present work, the ability of the first order turbulence model, employed in our computations, to model the formation of the counter-rotating-vortex pair (CVP) that appears in the flow-field was investigated. Computational results were in good agreement with experimental measurements. The effectiveness of such control actuator was tested on separated boundary layer. Preliminary investigation were presented and discussed.

INTRODUCTION

Synthetic jet actuators have been shown to be a useful tool for flow control, with applications including mixing enhancement, separation control, and thrust vectoring.
Methods for flow control can be broadly classified into two groups: passive or active. Passive (or fixed) control systems include riblets (Rohr et al. 1989, Djenini et al. 1994, Stephens et al. 1995, Bechert et al. 1997), large-eddy break-up devices (Andreas and Watson 1985), vortex generators (Bushnell and Moore 1991, McCormick 1992), castellation (Magi and Gai 1998), lobing (McCormick and Bennett 1994), and passive cavities (Jeng and Payne 1995). These systems are typically optimized for a narrow range of flow conditions and cannot adapt to changes in the incoming flow. Active (or variable) control systems include deforming surfaces (Chandrasekhara et al. 1997, Pal and Sinha 1998), variable velocity jets (Zhang 1995, Roberts et al. 1998), pulsed jets (Bremhorst and Hollis 1990, Williams et al. 1992, McManus

and Magill 1996), active suction (Gad-el-Hak 1994) and bleed (Bearman 1967, Marthur and Dutton 1995).

More recently, synthetic jets have been discovered as efficient actuators for flow control. The unsteady aspect was so important that in some experiments the continuous component of the synthetic jet has been even suppressed - hence some suction effects were added. The separation of boundary layers on cylinders or wings could be delayed, hence generating lift, with actuators located at the wall underneath the flow.

Eventually, this approach would permit the improvement of the flight response of aircraft without geometry changes of wings profiles.

The governing parameters for synthetic jets based on a simple "slug" model include a dimensionless stroke length $\frac{L_0}{d}$ and a Reynolds number based on the velocity scale:

$$U_0 = f\,L_0 = f\int_0^{T/2} u_0(t)dt \tag{1}$$

where $u_0(t)$ is the spatial-averaged velocity at the exit, $T = \frac{1}{f}$ is the period, d is the width of the slot (or diameter of the orifice), and L_0 is the distance that a "slug" of fluid travels away from the orifice during blowing phase of the cycle or period (Fig. 1). The Reynolds number is then defined as:

$$Re_{U_0} = \frac{U_0 d}{\nu} \tag{2}$$

where $\upsilon = \frac{\mu}{\rho}$ is the kinematic viscosity.

The effective velocity or mean square velocity of the synthetic jet is defined as follow:

$$U_{eff} = \frac{1}{T}\sqrt{\int_0^T u_0^2(t)dt} = \frac{U_{0,max}}{\sqrt{2}} \tag{3}$$

Note that $L_0/d = U_0/(fd)$ is closely related to the inverse of the Strouhal number, which may be written as:

$$\frac{1}{St} = \frac{Ud/\nu}{\omega d^2/\upsilon} = \frac{Re}{S^2} \tag{4}$$

where S is the Stockes number:

$$S = \sqrt{\frac{\omega d^2}{\upsilon}} \tag{5}$$

and $\omega = 2\pi f$ is the radian frequency of oscillation of the diagram.

In that context, the simple case of a synthetic jet in quiescent air (Figure 1) has very recently received further attention. It constitutes a separate and entire benchmark for numerical studies as well as for experimental investigation, because of a wide range of both injector and flow parameters that govern the jet behavior. These include the Reynolds numbers of the blowing, the Strouhal number of the actuation, the relative stroke-length and the shape of the velocity profile at the jet exit.

Synthetic jet dynamic was largely investigated using different flow measurement techniques including Particle Image Velocimetry, hot-wire anemometry, Laser Doppler Anemometry…etc. Two main technologies are emerged based respectively on piezoelectric actuator stimulated at resonance frequency (more than 1 kHz), extensively studied by Glezer and collaborators and on electrodynamic actuator having wide range of low actuation frequencies tested by Béra et al.

Numerical of high frequency actuation synthetic jet are widely performed by Kral et al. (1997). All works noted good agreement with the experimental data of Smith and Glezer obtained with piezoelectric devices.

In the present study, a low frequency synthetic jet in quiescent flow is investigated using numerical method. Results were compared to experimental measurements. The flow dynamic dominated by counter-rotating-vortex pair (CVP) induced by the actuator on the control of separated boundary layer problem. The mean effect of the generated CVP structures was illustrated which is essential for the success of future analysis of its interaction with the external flow.

DESCRIPTION OF THE GEOMETRY

The computational domain extends $160\ mm$ in the stream-wise direction and $80\ mm$ in the transverse direction. A $\frac{Quad}{Map}$ structured mesh with 14700 cells was employed here with a refinement near the edge of the slit (Figure 2). Following Kral et al., the actuator was modeled as a boundary condition for the velocity normal to the slit opening:

$$u(t) = U_{0,max} \sin(2\pi f t) \qquad (6)$$

where $U_{0,max}$ is the maximum jet velocity generated set at $6\ (m/s)$ and f is the actuation frequency which corresponds to $100\ Hz$. The velocity distribution is assumed to be top-hat function across the edge of the slit. In all simulations the flow was considered turbulent at $Re_j = 1360$ and $St_j = 0{,}02$.

COMPUTATIONAL METHOD

Unsteady incompressible numerical simulations were performed using the commercial code FLUENT 6.3.26. The Realizable $k-\epsilon$ model was selected based on the code documentation. This solver employs a second order accurate Upwind scheme for the spatial discretization and an implicit fractional step scheme for time advancement. The time step used in the computations was based on the global time step integration scheme. The time step was set at $2{,}77 \times 10^{-5}\ (s)$. The number of iterations for a cycle was 7200 and up to 3 cycles were simulated. Velocity/pressure coupling was ensured by the segregated PISO algorithm.

RESULTS AND DESCUSSION

Flow field details. The averaged velocity fields of both computational and experimental results during the blowing/suction cycle are shown in Figure 4. A relatively good symmetry of the field with respect to the injection plane can be observed. The basic steady fields (blowing and suction) provide two different flow structures. On the one hand, blowing generates a conventional jet normal to the wall, with regular spreading of the main flow and high entrainment of the surrounding fluid initially at rest. On the other hand, sucking generates an omnidirectional stream toward the slit. During the blowing phase, the fluid is pushed away sufficiently far from the slit so that it can later escape while the suction phase. Naturally, the resulting mean flow structure is different from that of a conventional steady jet (Figure 4). The mean velocity on the jet centerline shows a saddle point (at $X/h = 2$) where the mean effect of suction compensates for the mean effect of blowing. Above the saddle point, the mean velocity field looks like that of a conventional steady jet.

Comparison with experimental cases was made with already existing results (Congrès français de mécanique: Aloui et al.). A value of operating frequency was fixed at $100\ \mathbf{Hz}$ and a forcing amplitude of $8\ \mathbf{V_{cc}}$ was considered.

In order to compare the different flow structures, we focus on the velocity profile in the usual similarity coordinates, using $\frac{Y}{b}$ and $\frac{U}{U_{cl}}$ (Figure 3). The half-width b is defined as the lateral distance at which the mean jet profile is reduced to half of its maximum velocity U_{cl} at the same axial section.

For the mean velocity profile, a good agreement is observed between experiment and the computation. The curves indicate a slight symmetry and self-similarity of both PIV and computational profiles. Moreover, there is a broad agreement between the trends for the measured and computed mean velocities. Close to the injection slit, the computational and experimental profiles show a strong central peak. But while moving upward the slit, the maximum decreases and the profiles become flatter in central region of the jet. This put the emphasis on the spreading turbulence induced by the synthetic jet as the flow proceeds away from the slit. A remarkable feature, however, is the presence of negative U/U_{cl} velocities for $|Y|/b \geq 1$ that occurs in both computational and experimental profiles.

This is due to the association of the large rotating secondary flows with the entrainment effects in the ambient air. This property is more visible while dealing with phase-averaged velocity maps for both numerical and experimental cases represented in figure 5. These maps illustrate the presence of pairs of counter-rotating eddies, which develop and move downstream over the injection cycle.

Detection of the vortex centres. The eddy structures obtained using the Γ_1-criterion. This criterion is based on the concept of angular momentum (M.A.N) and is presented by a dimensionless function defined at a point P as:

$$\Gamma_1(P) = \frac{1}{S}\int_{M\in S} \frac{\left(\overrightarrow{PM} \wedge \vec{U}(M)\right)}{\left\|\overrightarrow{PM}\right\| . \left\|\vec{U}(M)\right\|} \overrightarrow{dS} = \frac{1}{S}\int_{M} \sin\theta_M dS \qquad (7)$$

Figure 6 shows eddies detected by the Γ_1-criterion. These maps provide the evolution of vortex structures during an excitation cycle of the actuator.
During its growth, the counter-rotating-vortex pair (CVP) sucks up air from the surrounding area. According to the initial findings, fluid supply is provided by convection of two mixing layers. Therefore, the two vortex structures remain symmetrical during the entire period of actuation. At the end of the blowing phase, there is a significant deceleration of the vortex pair evolution. This can be explained by the switch to aspiration process. Indeed, the aspiration limits the sprawl of vorticity rings because it lacks feeding fluid. A sort of competition takes place between the two aspirations: the slit and the vortex ring.

Fluctuating kinetic energy. The maps of the iso-kinetic energy contours given by both computations and experiments are shown in Figure 8. The contours of computational velocity fluctuations seem to be in poor agreement with those provided by experiments. In terms of fluctuating magnitudes, the computed synthetic jet flow generates larger fluctuating kinetic energy than the experimented one. This discrepancy is likely due to imperfections of the PIV measurements device. However, transverse expansion of fluctuations contours presents some similarity for both computational and experimental approaches.
Obviously, the synthetic jet actuator generates intense fluctuations near the shearing zones or the jet development regions (Figure 7). This feature highlights the ability of a synthetic jet to energize low fluctuating kinetic energy level flows such as wakes or recirculation zones.
Trajectories of the vortex centers Figure 9 shows the mean trajectory covered by instantaneous positions of the vortex centers in steps of $10°$ of phase-angle of the blowing/suction cycle.
At its beginning, the trajectory is roughly defined by approximately parallel vertical mean line up to $Y/h = 30$ from the slit: this correspond to the stage of vortex formation.
The convection velocity of the vortices can be deducted from vortex locations and the actuator frequency.

POD post-processing. The Proper Orthogonal Decomposition is an efficient tool for coherent structures extraction. It's based on the decomposition of the fluctuating velocity in a combination of spatial deterministic eigenfunctions (or modes) $\phi_n(x)$ weighted by the temporal coefficients $a_n(t)$:

$$\vec{U}(\vec{x},t) = (\vec{U}(\vec{x},t)) + \sum_{n=0}^{\infty} a_n(t)\phi_n(\vec{x}) \qquad (8)$$

As part of this study, eigenfunctions $\phi_n(x)$ are computed using the "snapshots" method. The number of eigenfunctions computed using 36 snapshots of an actuation cycle are uniformly spaced in order to establish comparison with experimental phase-averaged fields. Afterwards, each eigenvalues (or proper values) λ_n is associated to the energy weight of each eigenfunctions $\phi_n(x)$.

In this study, the POD analysis of the 36 phase fields indicates that the synthetic jet flow can be represented by a reduced order model based on the first four eigenfunctions which contain roughly 95% of the total energy against 93% for experimental measurements (Table 1). These eigenfunctions correspond to the high-energetic large-scale structures. The first eigenfunction clearly have the most energy at the jet exit. This means that the largest velocity fluctuations take place in this region. The second pair of eigenfunctions has also a substantial amount of energy. They are also large eddy-structures.This slight difference between computational and experimental energy rate for the first four eigenfunctions is mainly due to experimental noise. These four eigenfunctions represents the convective behavior of the CVP structures from its creation to its vanish during an actuation cycle. Both figure 10 & 11 put emphasis on the efficient reproduction by the CFD modeling of the coherent structures mechanism that characterize the synthetic jet flow.

PARAMETRIC STUDY

This part of the study focuses on the flow-field generated by the synthetic jet in different situations. Both computational and experimental results will be discussed within a parametric characterization of the flow features submitted to a variety of forcing boundary conditions imposed on the exit of the injection slit.

The effect of the amplitude. Figure 11 shows the evolution of the maximum centerline velocities of both computational and experimental case. While keeping the forcing frequency constant at $100\ \mathrm{Hz}$ and the phase at $90°$, the mean centerline velocity indicates an increasing values according to the variation of the forcing amplitude . A good agreement between computational and experimental curves is observable for higher voltages. Beyond $10\ V_{cc}$, experimental U_{cl} begins decaying dramatically. This may be due to the limited performances of the loudspeaker.

The effect of the frequency. The variation of the mean velocity with frequency is shown in Figure 12. The forcing amplitude was kept constant at $8\ V_{cc}$ and the phase was fixed at $90°$. The variations for both computational and experimental configurations exhibit broadly similar features while dealing with frequencies smaller than 100 Hz. The resonance frequency of the membrane, which corresponds to the peak, is approximately $100\ Hz$.

The operating frequency of the actuator was found to have little effect on the accuracy of the velocity magnitude while dealing with the computational case. However, the lower value of the frequency indicated a higher instability in the external flow pattern. This behavior of the solution may also be related to the insufficient mesh point in the near orifice region and the incorrect modeling of the actuator boundary condition.

SYNTHETIC JET ACTUATOR IMPLEMENTATION ON SEPARATED BOUDARY LAYER FLOW

To investigate the implementation of synthetic jet actuator for boundary layer separation control, the basic configuration of an asymmetric two-dimensional diffuser was considered. This configuration was a test-case for the 8th ERCOFTAC/IAHR/COST workshop on Refined Turbulence modeling in Espoo, Fineland, 17-18 June 1999. A number of experimental studies were carried out with this geometry including Buice and Eaton. The present work aims to reproduce Buice and Eaton's work computationally focusing on the effectiveness of adding periodic actuation at the diffuser entrance for delaying boundary layer separation. The principal effort is centered on qualitative computation to better understand the relevant mechanism of flow-structures interaction involved.

The diffuser apparatus can be divided into three sections: an inflow channel, the asymmetric diffuser, and an outflow channel. Buice and Eaton used the channel height, $H = 0.591$ inches, as their reference length. The inflow channel section has a length of $110H$. The diffuser has a 10 degree expansion angle and is $21H$ in length. At the end of the expansion, the diffuser channel is $4.7H$ in height. The axial station corresponding to the beginning of the expansion section is set as $\frac{x}{H} = 0$.

Two-dimensional, structured, computational grids were generated for all cases using Gambit software. A $\frac{\text{Quad}}{\text{Map}}$ structured mesh with 35992 cells was employed here with a refinement near the edge of the diffuser (wall spacing set to $y+ = 0.2$). The diffuser inlet flow is a two-dimensional, turbulent, and fully-developed channel flow with a Reynolds number of $20\,000$ based on the centerline velocity and the channel height. The fully developed channel centerline velocity was $20\frac{m}{s}$ and a $k-\omega$ SST turbulence model was employed.

The synthetic jet actuator, located $1\mathbf{mm}$ away from the primary jet exit on the lower wall of the diffuser, was used to produce the periodic excitation. The maximum velocity at the actuator exit corresponds to $32\frac{\mathbf{m}}{\mathbf{s}}$ and an operating frequency of $100\ \mathbf{Hz}$ was fixed (as tested by Ben Cheikh et al.2003).

The visualization of the streamlines in both uncontrolled and controlled diffuser (Figure 13 & 14) shows that the use of periodic actuation (synthetic jet) can significantly delay the boundary layer separation length in the lower wall of the diffuser. This indicates the ability of the synthetic jet actuator for resuscitating recirculation zones with CVP eddies generation. Accordingly, the introduction of such instabilities in the flow will significantly enhance heat transfer with eventual heated surface. A thorough investigation is planned.

CONCLUSION

The flow generated by a low actuation frequency based on synthetic jet technology has been investigated. As observed in experiment, computational results illustrated the turbulent behavior of the jet, the large expansion of the jet and the large entrainment rate of surrounding fluid. The synthetic jet dynamic was based on the generation of a counter-rotating-vortex pair (CVP) during the blowing phase and its self-induced convection during the suction phase. This feature was approved by the POD analysis. Broadly speaking, the performed comparison between computation and experiment approves the capability of Realizable $k-\varepsilon$ in modeling the dynamic of the synthetic jet actuator.

Preliminary results of the implementation of this device on separated flow in asymmetric diffuser have been obtained. Significant modification of the flow behavior was illustrated which represent a promoting characteristic in enhancing convective heat transfer between heated surfaces and external flows.

REFERENCES

Mallinson S.G., Hong G. and Reizes J.A., "*Some characteristics of synthetic jet*", AIAA paper 99-3651, 1999.

Yogan U., Holman R., Mittal R., Carol B., Sheplak M., and Cattafesta L., "*A jet formation criterion for synthetic jet actuator*", AIAA paper 2003-0636.

Catalin N., "*Numerical simulation of a synthetic jet actuator*", National institute for Aerospace Research ICA0266.1.

Kral. L.D., Donovan J.F., Cain A.B., and Cary A. W., "*Numerical simulation of synthetic jet actuators*", AIAA paper 97-1824.

Béra J.C., Michard M., Grosjean N. and Comte-Bellot G., "*Flow analysis of two-dimensional pulsed jets by particle image velocimetry*", Experiments in fluid, Vol.31, n° 5, pp. 519-532.

Ben Chiekh M., "*Contrôle d'écoulements par jets synthétiques: Analyse à partir de mesures de Vélocimétrie par Image de Particule*", Thèse de doctorat 2003. Ecole Nationale d'Ingénieurs de Monastir.

Dghim M., "*Simulation numérique du contrôle par jets synthétiques des écoulements décollées*", PFE 2008. Ecole Nationale d'Ingénieurs de Monastir.

Aloui F., Ben Chiekh M., Ben Nasrallah S. and Kourta A., "*Caractérisation d'un jet synthétique en vue de son utilisation pour le contrôle*'',18ème Congrès Français de Mécanique, Grenoble 27-31 août 2007.

Obi, S., Aoki, K., and Masuda, S., "Experimental *and Computational Study of Turbulent Separating Flow in an Asymmetric Plane Diffuser*",Ninth Symposium on Turbulent Shear Flows, Kyoto, Japan, August 16–19, pp. 305–1 to 305–4, 1993.

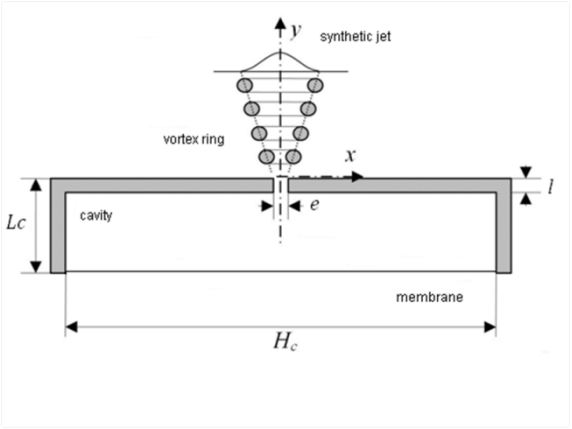

Figure 1. Schematic of a synthetic jet

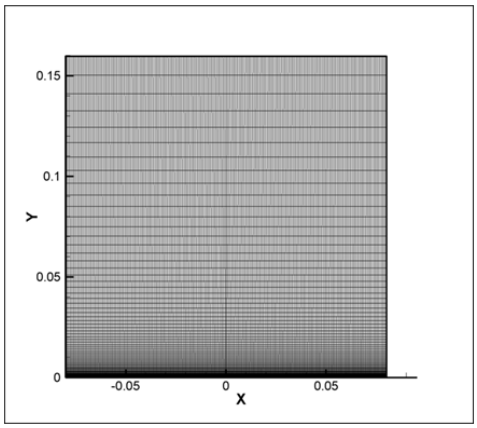

Figure 2. Fixed structured Cartesian grid

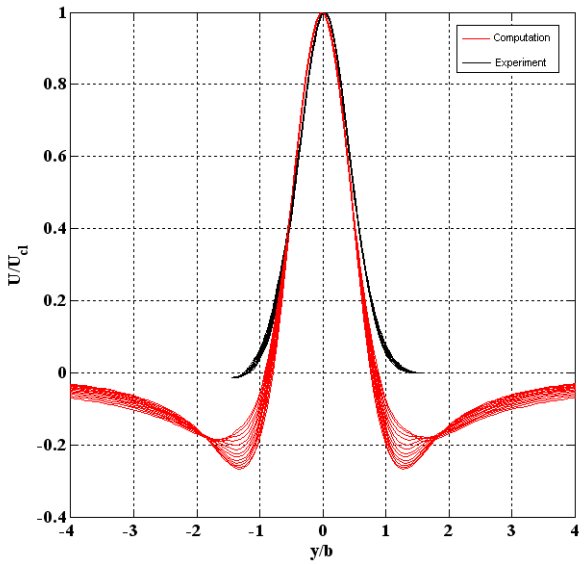

Figure 3. Jet centre-line mean velocity profiles

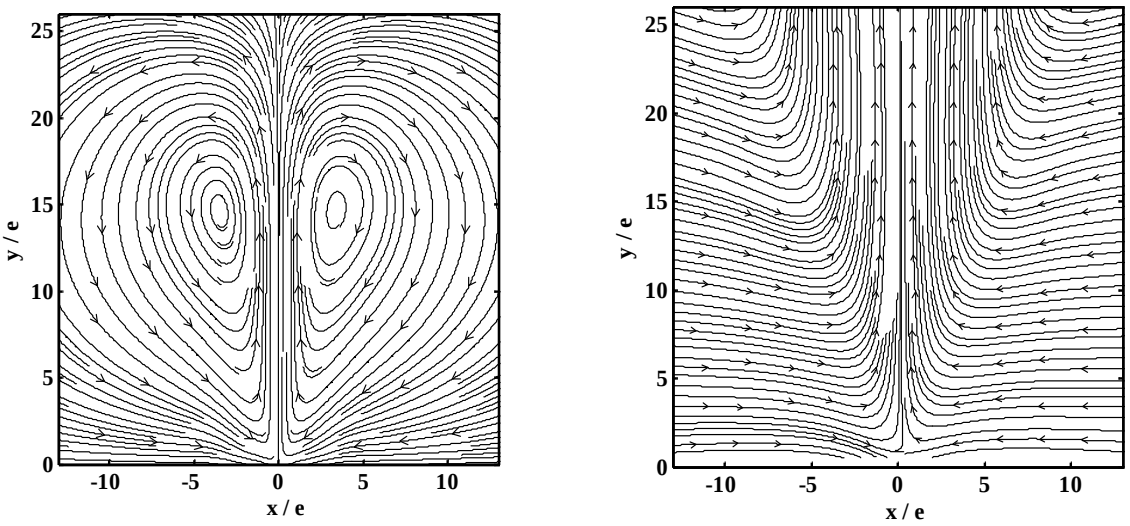

a) b)

Figure 4. Mean velocity streamlines: a) computational case, b) experimental case

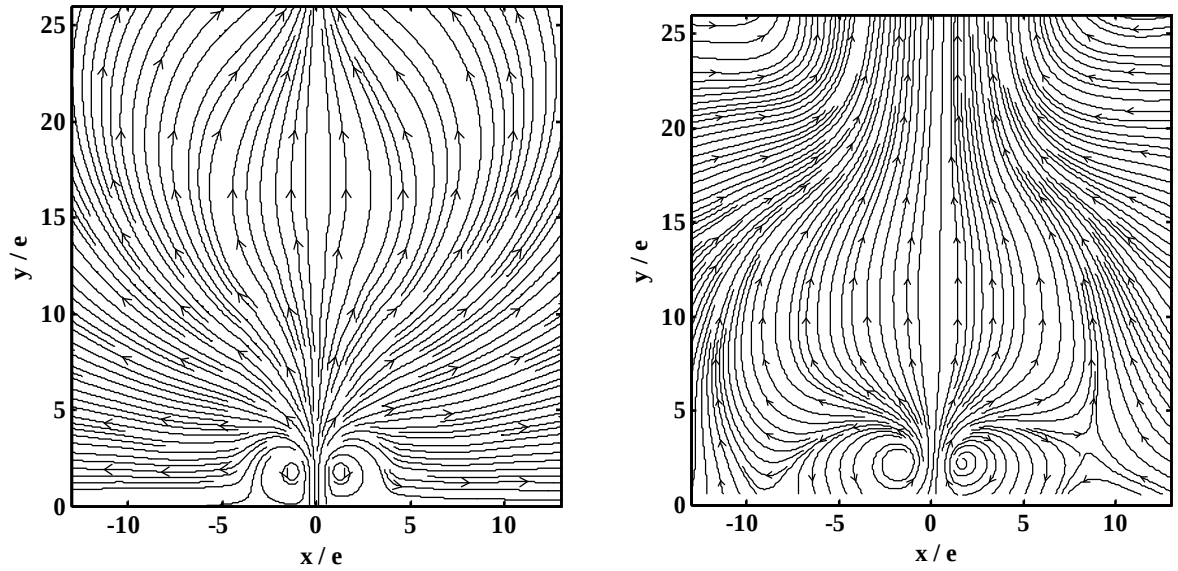

Beginning of blowing

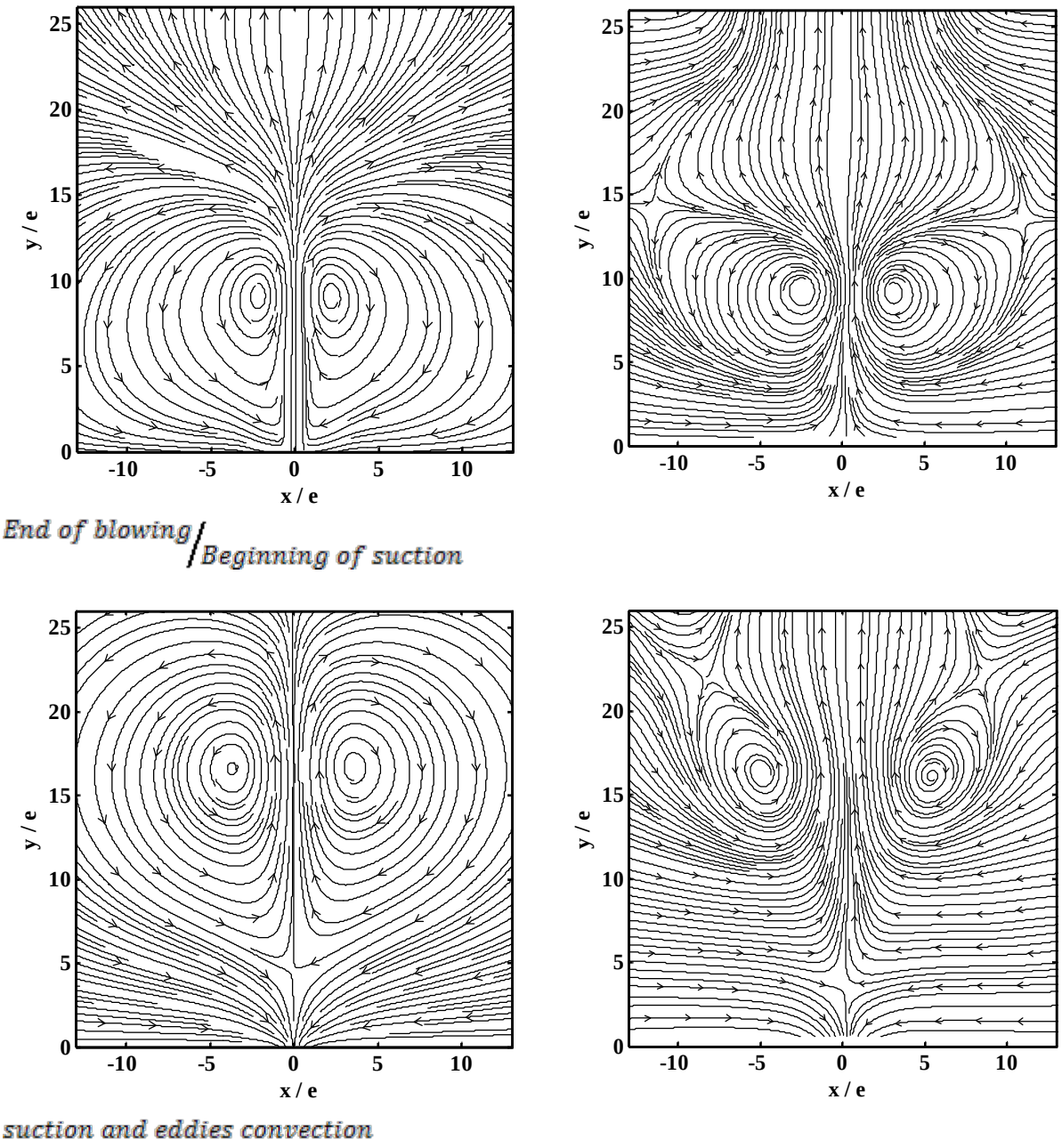

a) b)

Figure 5. a) Time sequence of computational velocity streamlines during an actuation cycle
b) Experimental phase-average velocity streamlines during an actuation cycle

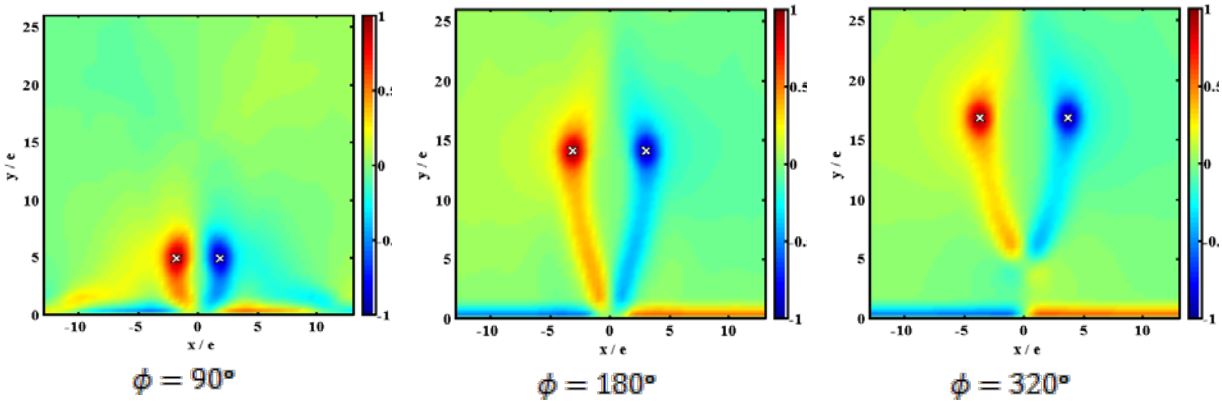

Figure 6. Γ_1-criterion maps for different phases of the blowing/suction cycle

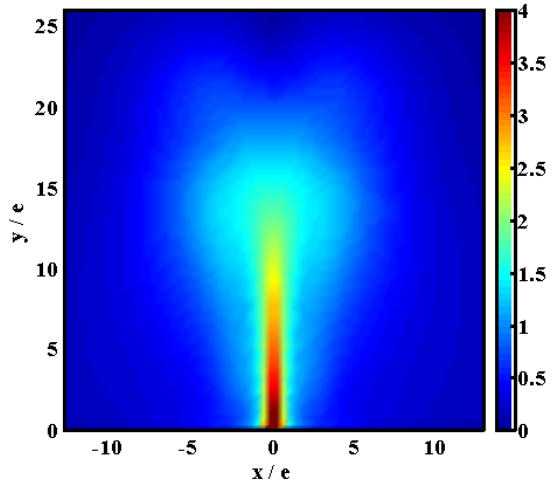

Figure 7. Fluctuating Kinetic energy map provided by computation

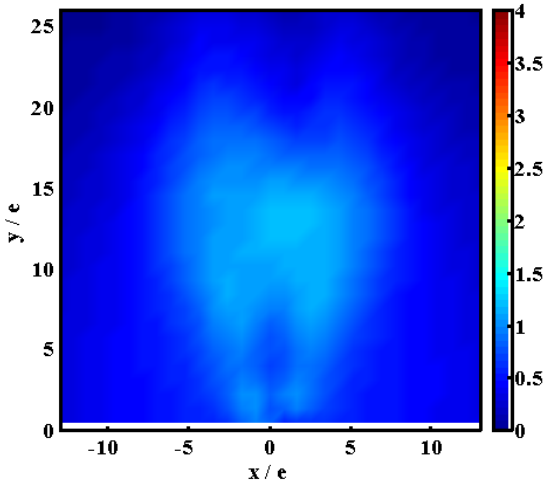

Figure 8. Fluctuating Kinetic energy map provided by experiment

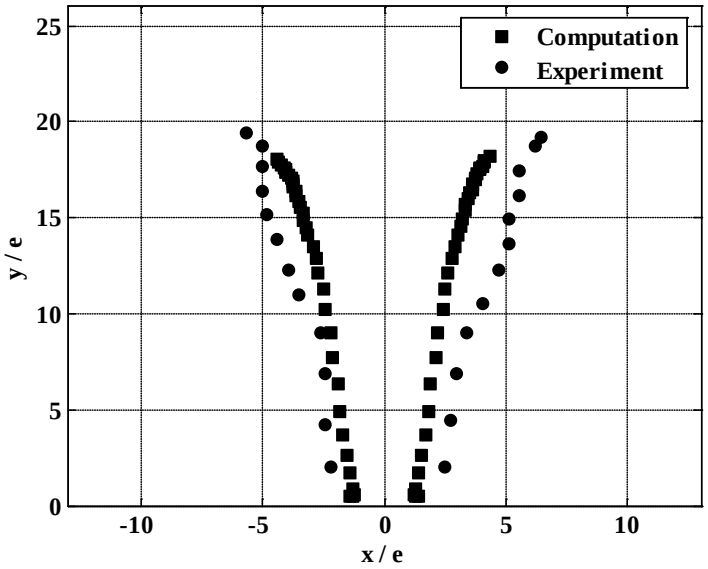

Figure 9. Locations of vortex centers during an actuation cycle

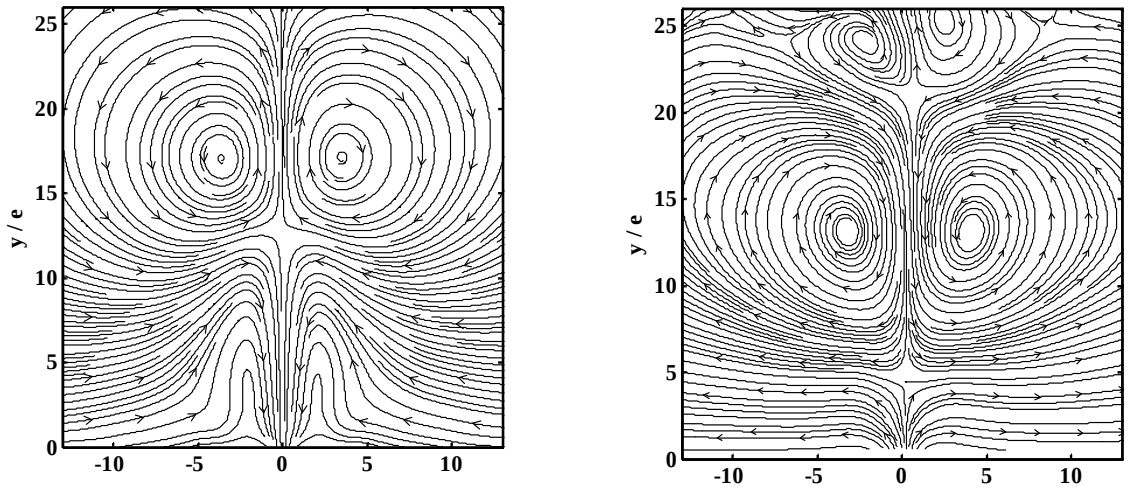

a)

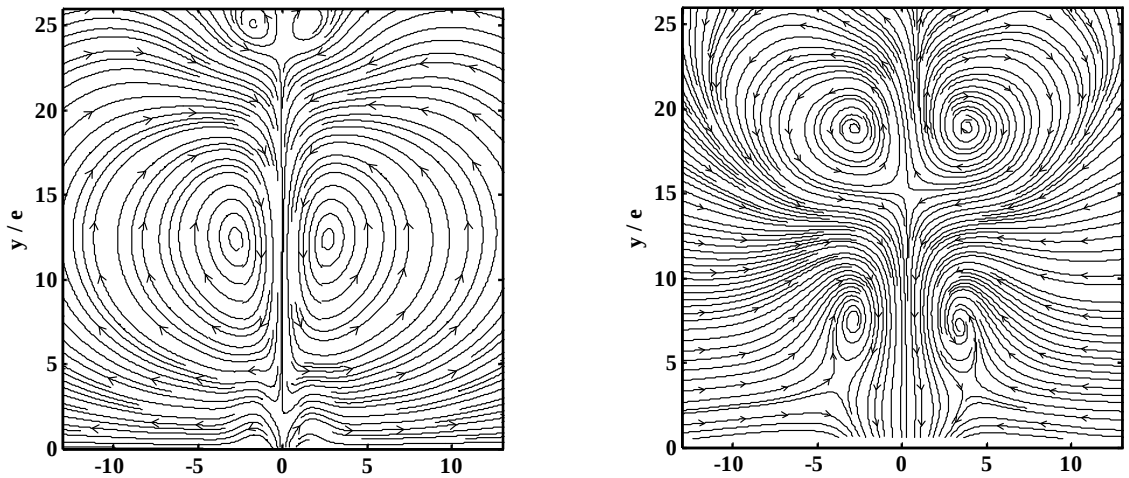

b)

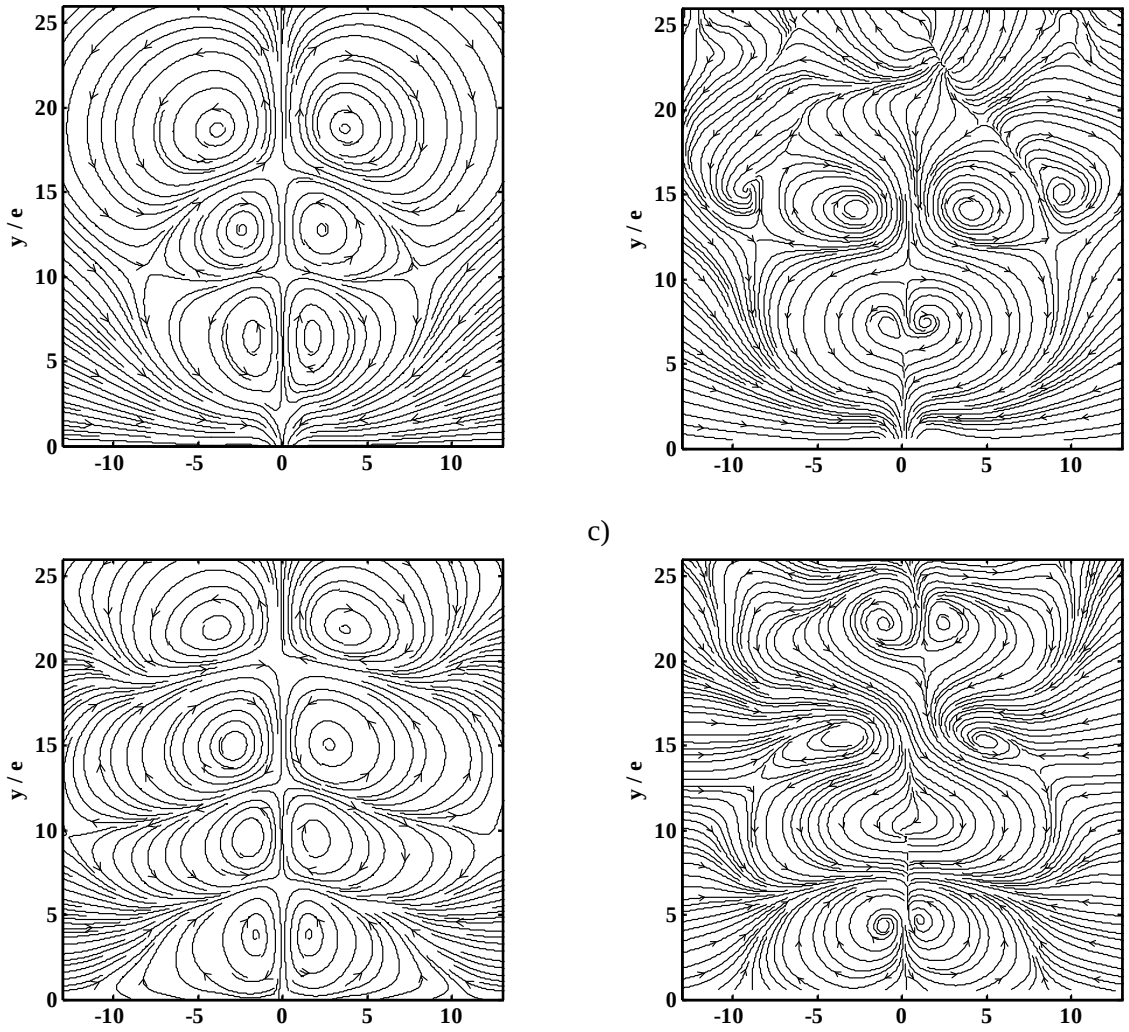

Figure 10. Vector plots of the velocity of the first 4 experimental POD eigenfunctions: a) eigenfunction 1, b) eigenfunction 2, c) eigenfunction 3, d) eigenfunction 4

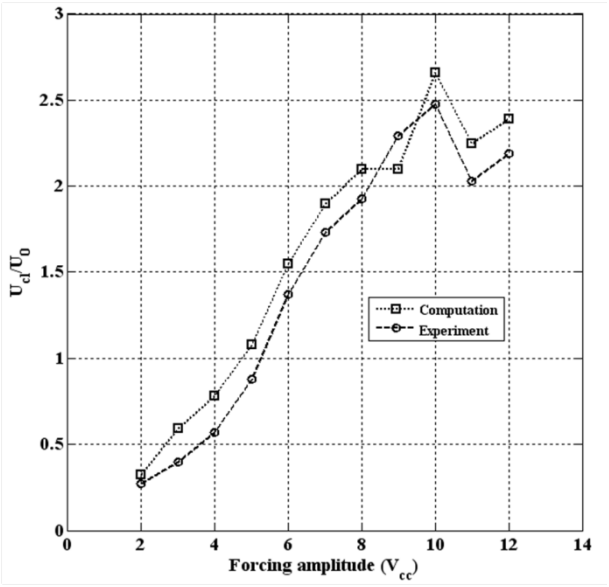

Figure 11. Maximum centerline velocity vs. actuation amplitude

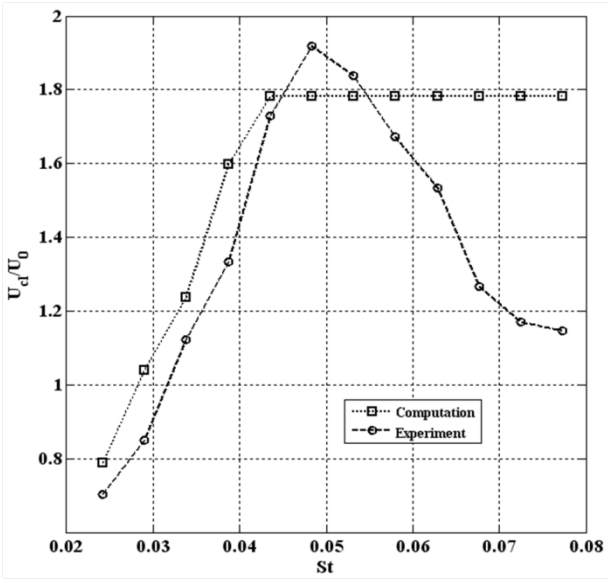

Figure 12. Maximum centerline velocity vs. actuation Strouhal number

Table 1.

Energy weight associated to each eigenfunction (mode)

Mode n°	Computation	Experiment
1	52.0990	44.8687
2	31.0655	35.6030
3	6.9160	7.6394
4	4.7275	5.1379
Total Energy	94.8080	93.2490

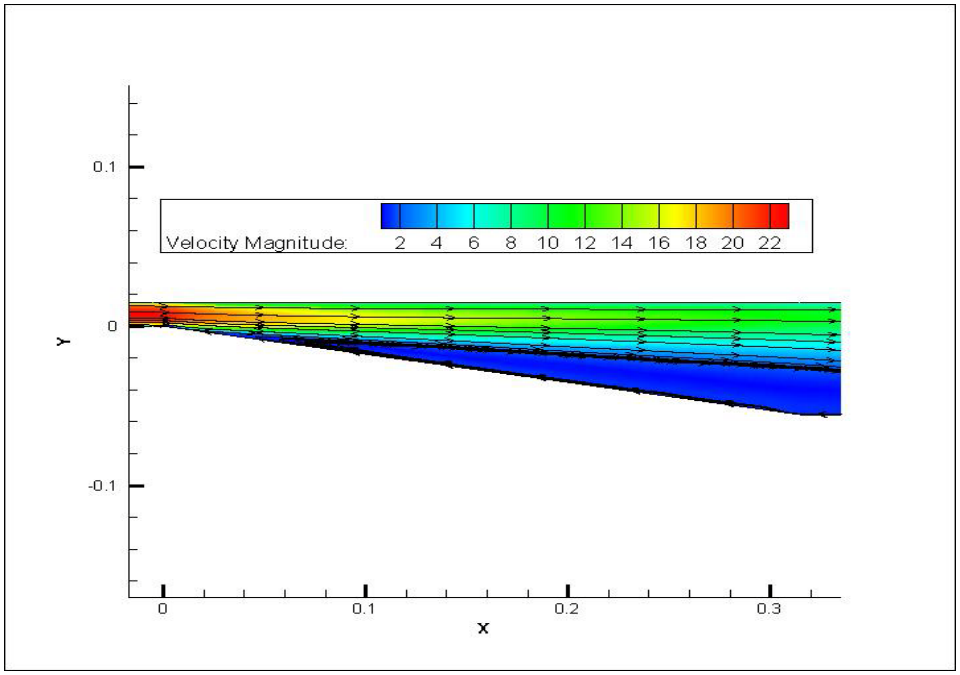

Figure 13. Streamlines with contours of axial velocity showing separated flow SST model (without control).

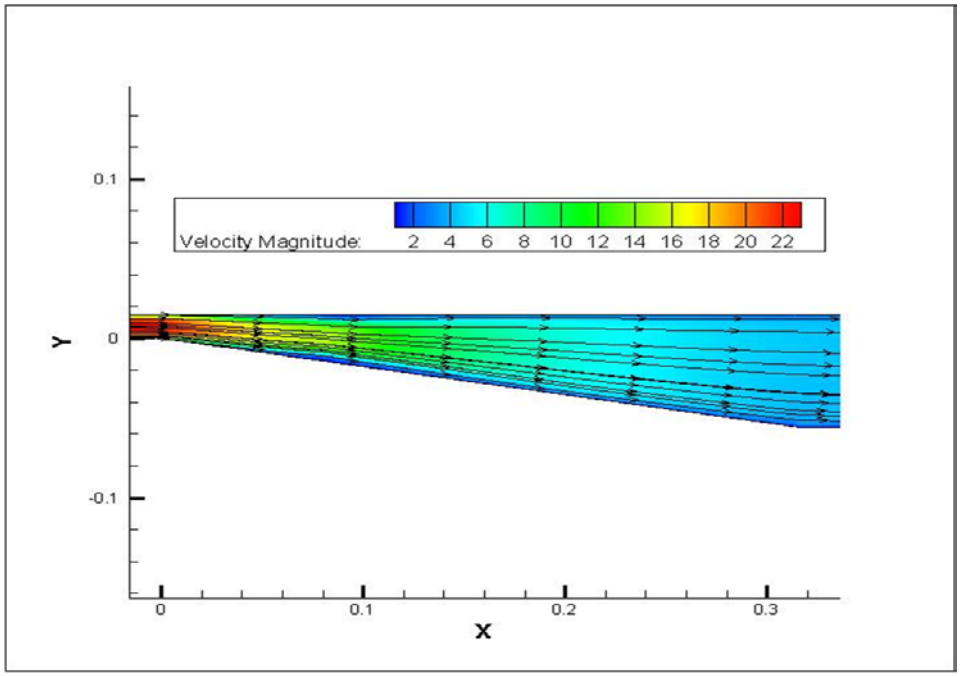

Figure 14. Streamlines with contours of axial velocity showing separated flow SST model (with control).